

Published in final edited form as:

*Nanotechnology*. 2010 April 30; 21(17): 175702. doi:10.1088/0957-4484/21/17/175702.

## Trajectory control of PbSe- $\gamma$ -Fe<sub>2</sub>O<sub>3</sub> nanoplatforms under viscous flow and an external magnetic field

Lioz Etgar<sup>1</sup>, Arie Nakhmani<sup>2</sup>, Allen Tannenbaum<sup>2,3</sup>, Efrat Lifshitz<sup>1,4</sup>, and Rina Tannenbaum<sup>1,5,6</sup>

<sup>1</sup>Russell Berrie Nanotechnology Institute (RBNI), Technion—Israel Institute of Technology, Haifa 32000, Israel

<sup>2</sup>Department of Electrical Engineering, Technion—Israel Institute of Technology, Haifa 32000, Israel

<sup>3</sup>School of Electrical and Computer Engineering, Georgia Institute of Technology, Atlanta, GA 30332, USA

<sup>4</sup>Schulich Faculty of Chemistry, Technion—Israel Institute of Technology, Haifa 32000, Israel

<sup>5</sup>Department of Chemical Engineering, Technion—Israel Institute of Technology, Haifa 32000, Israel

<sup>6</sup>School of Materials Science and Engineering, Georgia Institute of Technology, Atlanta, GA 30332, USA

### Abstract

The flow behavior of nanostructure clusters, consisting of chemically bonded PbSe quantum dots and magnetic  $\gamma$ -Fe<sub>2</sub>O<sub>3</sub> nanoparticles, has been investigated. The clusters are regarded as model nanoplatforms with multiple functionalities, where the  $\gamma$ -Fe<sub>2</sub>O<sub>3</sub> magnets serve as transport vehicles, manipulated by an external magnetic field gradient, and the quantum dots act as fluorescence tags within an optical window in the near-infrared regime. The clusters' flow was characterized by visualizing their trajectories within a viscous fluid (mimicking a blood stream), using an optical imaging method, while the trajectory pictures were analyzed by a specially developed processing package. The trajectories were examined under various flow rates, viscosities and applied magnetic field strengths. The results revealed a control of the trajectories even at low magnetic fields (<1 T), validating the use of similar nanoplatforms as active targeting constituents in personalized medicine.

### 1. Introduction

Several important attributes typify active targeting moieties. They should administer tags or drugs precisely to afflicted cells, leaving the healthy tissues unaffected [1,2]. Furthermore, they should be amenable to visualization, following their fluorescence [3–5], or to magnetic resonance imaging [6–9]. Active targeting moieties should also be soluble in aqueous media, stable to fluctuations in the pH of their physiological environment and under various flow conditions. Although beyond the scope of this work, well-planned targeting complexes should be able to selectively discharge a therapeutic drug, and eventually be effectively eliminated from the body upon completion of their function.

To address this challenge, we developed novel nanostructure clusters that constitute basic nanoplatforms, to which the various functions (e.g. drug administration) could potentially be

tethered. These clusters were created by the chemical conjugation of water-soluble PbSe colloidal quantum dots (QDs) to superparamagnetic  $\gamma$ -Fe<sub>2</sub>O<sub>3</sub> nanoparticles (NPs), bonded via selective interactions between complementary functional groups [10–16]. The magnetic NPs serve as transport vehicles, manipulated by an external magnetic field gradient, and the QDs act as fluorescence tags with an optical window in the near-infrared regime.

The QDs exhibit characteristic electronic and optical tunability that vary according to their size. Currently, PbSe QDs are the focus of extensive attention due to their distinctive intrinsic properties [17–19], showing well-defined band-edge excitonic transitions tuned between 1 and 3.5  $\mu\text{m}$  emission with an optical penetration depth in living tissue of 5–10 cm [20,21], a relatively large ground-state cross section of absorption ( $\sim 10^{-15} \text{ cm}^{-2}$ ), long excitonic lifetime at room temperature (400–500 ns) and exceptionally high room temperature luminescence quantum efficiency ( $\sim 80\%$ ) [11,12,22], altogether making them a model of *in vivo* fluorescing tags [15,16,23]. Awareness regarding the toxicity of lead QDs exists; however, this study uses them as a model case, while practical applications would require their replacement by a less toxic material (with similar fluorescence properties), or the development of a biocompatible surface coating for the QDs.

The magnetic responsiveness of the  $\gamma$ -Fe<sub>2</sub>O<sub>3</sub> moiety within the nanoplatfoms is related to a remote manipulation of their motion by an externally applied magnetic field, actively enhancing their accumulation in a target surrounding, while explicit bonding to a cell is driven by chemical functional groups (attracted by complementary cell receptors). The clusters join a group of other magnetic nanostructures, working as therapeutic drug carriers that target specific sites in the body [24–26]. Together, such nanoplatfoms constitute a drastic change, departing from the more common passive targeting methods, offering preferential partition of drugs administered into highly vascular tissues [27–34]. It should be noted that the  $\gamma$ -Fe<sub>2</sub>O<sub>3</sub> NPs themselves can serve as magnetic tags in magnetic resonance imaging; however, the most recent method using these magnetic tags is known as a relatively expensive medical diagnostic tool, with a spatial resolution of  $\sim \mu\text{m}$ . In contrast, fluorescence tags with high quantum efficiency should offer an improved spatial resolution down to a submicron for utilization in the human body with a ppb concentration [35]. Thus, the  $\gamma$ -Fe<sub>2</sub>O<sub>3</sub> NPs are utilized here only as a transport vehicle.

Other than the development of novel magnetic cargo, there is very little information about the dynamic behavior of nanoplatfoms under conditions that are similar to the environment found in blood vessels [36–42]. Thus, the motion of the newly developed QD–NP nanostructure clusters ( $\sim 30 \text{ nm}$  in size) in a viscous fluid flow is of crucial importance. This document describes the transport properties of the QD–NP nanoplatfoms when examined under different fluid flow rates (capacitances) and several fluid viscosities (mimicking the viscosity of blood), while applying an external magnetic field. All the flow experiments were conducted with the nanoplatfoms' suspension in aqueous poly(ethylene glycol) (PEG) solution, recorded by a CCD camera. The resulting video films were analyzed by a unique software package, supplying the direction and velocity of the trajectory of each QD–NP cluster.

## 2. Results and discussion

### 2.1. Synthesis and characterization of PbSe QD- $\gamma$ -Fe<sub>2</sub>O<sub>3</sub> NP nanoplatfom

The pure PbSe QDs and the  $\gamma$ -Fe<sub>2</sub>O<sub>3</sub> NPs, with a typical diameter of  $\sim 5 \text{ nm}$ , were synthesized by colloidal procedures (see section 4). The PbSe QDs were functionalized by 2-aminoethanethiol (AET) surfactants, with the amino groups facing the exterior periphery. The  $\gamma$ -Fe<sub>2</sub>O<sub>3</sub> NPs were functionalized by hydrophilic polyhedral silsesquioxane (PSS) ligands, containing eight SiO<sup>-</sup> functional groups. A mix of equivalent amounts of QD and NP constituents in solutions with pH between 5 and 7.5 permitted a ligand–ligand interaction via

two different hydrogen bonds between  $-\text{NH}_3^+$  and  $-\text{SiO}^-$  and  $\text{CH}_2-$  and  $-\text{SiO}^-$  chemical groups (see figure 1(A)), as proved by the NMR investigations (not shown) and energy minimization calculation [14, 43]. Figure 1(B) represents a transmission electron microscope (TEM) image of PbSe QD- $\gamma$ -Fe<sub>2</sub>O<sub>3</sub> NP nanoplatfoms, deposited onto a TEM grid from the acidic solution at pH  $\sim$  5, showing clustering of particles into a platform with an average size of  $30 \pm 10$  nm (including  $\sim$ 10 QDs and 10 NPs). A corresponding electron diffraction pattern, shown in the inset, reveals the existence of PbSe (space group  $Fm\bar{3}m$ ) and  $\gamma$ -Fe<sub>2</sub>O<sub>3</sub> (space group  $P4_132$ ) particles within a cluster. Further on, a zoomed view over a single nanoplatfom (not shown) reveals distinctive lattice fringes of the individual QDs and NPs, with a surface-to-surface distance of 1.3 nm between adjacent particles, in good agreement with the combined AET-PSS molecular length, supporting the formation of a hydrogen bond as mentioned. A previous study [43] revealed that the hydrogen bond is stable in solutions with a pH of  $\sim 7 \pm 2$ , while deviation from this condition dissociates the QD-NP conjugation.

Figure 1(C) shows the continuous-wave photoluminescence spectra of PbSe NQD- $\gamma$ -Fe<sub>2</sub>O<sub>3</sub> NP nanoplatfoms (red curves) and of pure PbSe QDs with an average diameter of 5 nm (blue curves), recorded at room temperature. The spectra are composed of a single band, associated with the ground-state exciton emission. Representative absorption spectra of the pure PbSe NQDs and the corresponding QD-NP nanoplatfoms are shown in the inset of the figure. The emission and absorption bands of the nanoplatfoms are shifted by 12–14 meV with respect to the pure QDs. Our previous study [43] correlated this shift with the influence of the dielectric environment of the  $\gamma$ -Fe<sub>2</sub>O<sub>3</sub> NPs in the surroundings of the QDs, but excluded a direct electronic interaction (e.g. plasmon-exciton, exciton-exciton) due to a deviation of the plasmonic frequency, or the electronic band-edge of the NPs from that of the QDs. In any event, the  $\gamma$ -Fe<sub>2</sub>O<sub>3</sub> NPs do not quench the luminescence intensity of the PbSe QDs upon conjugation, making the QD-NP clusters suitable diagnostic nanoplatfoms.

The magnetic properties of the nanoplatfoms were examined by following the dependence of their susceptibility ( $\chi$ ) on the strength of the external magnetic field ( $H$ ) at different temperatures. Figure 1(D) shows a representative plot of this dependence, measured at room temperature and at 20 K, compared with that of the pure  $\gamma$ -Fe<sub>2</sub>O<sub>3</sub> NPs. The lack of the hysteric suggests the existence of superparamagnetism and the retention of this property within the QD-NP nanoplatfom.

## 2.2. Flow trajectory measurements

The flow measurements were carried out by suspending 10  $\mu\text{g}$  of QD-NP nanoplatfoms into six different aqueous poly(ethylene glycol) (PEG) solutions with the following viscosities: 1.25, 1.73, 2.13, 3.71, 4.13 and 6.35 cP. The flow of each solution was measured at several flow rates (0.03, 0.05, 0.1, 0.2, 0.3, 0.5, 0.7 and 0.9 ml h<sup>-1</sup>), with and without the influence of an external magnetic field. Control experiments were done by measuring the flow of pure PEG solutions of the same viscosities, operating under the same flow rates.

The solutions were injected into a 500  $\mu\text{l}$  sample chamber, which was placed within a beam path of a laser source. The nanoplatfoms were visualized through an optical microscope as small points of scattered light, and their instantaneous position was recorded by a CCD camera with a 10 s exposure duration. An electromagnet, with field strength between 0 and 1 T, was placed perpendicular to the chamber, distanced from the solution by  $\sim$ 5.5 cm, inducing a magnetic field gradient of 0.01–0.03 T at the center of the chamber. Figure 2(A) shows a photograph of the flow set-up, and additional experimental details are supplied in section 4. Figure 2(B) shows a schematic drawing of the nanoplatfom's motion in the  $x$ - $y$  plane through a chamber and under the influence of a magnetic field gradient. The nanoplatfoms are shown by the circles, their deviation from the chamber center is labeled by  $\theta$  and the magnetic field

is oriented perpendicular to the chamber axis. Figures 3(A)–C show representative images of nanoplateforms' trajectories as visualized during a flow, tracking the position change of the two selected nanoplateforms (see yellow circles in the figure).

### 2.3. Unique trajectory processing algorithm

A graphical user interface (GUI) was developed, implementing an algorithm discussed below, enabling automatic determination of the location of a nanoplateform from raw video data and construction of its trajectory. The GUI was developed with a MATLAB program. This GUI allows the user to tune different detection parameters, to choose visibility levels, activate filtering process and to save the extracted data for further statistical analysis (see section 2.4).

Figure 4 shows a GUI panel exhibiting three images on the screen (from left to right): an original noisy video image with a poor contrast, a filtered preprocessed image and binary decision image. A location of a detected nanoplateform is memorized as '1' (white) and the background pixels are memorized as '0' (black); a cross on the decision image marks a nanoplateform center of mass (named hereafter as centroid).

Actually, the GUI analyzes two-dimensional frames of three-dimensional trajectories, encountering difficulties with the appearance, disappearance and then re-appearance of a nanoplateform in a certain frame. The disappearance of nanoscaled particles during a flow was not dealt with appropriately until the present. Kachouie *et al* [44] developed an algorithm for a disc-shaped micron size biological cells, thus determining a low signal/noise ratio that is not suitable for our case. Acton *et al* [45] treated a flow of virus cells, following the trajectory of all particles at the same point in time, ignoring the appearance of new particles at a later time, which is not applicable to our case either since the appearance of new particles must be considered. Nakamura *et al* [41] and Helmuth *et al* [46] considered an average position of particles from five consecutive frames, still missing appearance/disappearance events.

This work developed a special procedure (see below) that overcomes the mentioned obstacles by consideration of the following points: (a) criteria for appropriate visibility conditions; (b) estimation of the direct velocity [47]; (c) automatic initiation and termination of nanoplateform tracks; (d) consideration of centroid tracking also of non-spherical nanoplateforms; (e) sequential order of frame processing (trajectory update is based on a current frame only); (f) novel approach of tracking by filtering [47], based on brightness and contrast correction. Four filtering processes were used: a low pass filter, a band pass filter, an image gradient filter and a gray level morphological filter. The filter parameters (such as bandwidth and cutoff frequency) were tuned with sliders located on the left preprocessing panel in the GUI (see figure 4). The result of the preprocessing stage is displayed in the middle image of figure 4. The program searches for the most prominent brightness peaks in the filtered image. All pixels with a brightness level higher than a specified threshold (defined by the user) become logic '1' in the binary decision image (left panel in figure 4). The binary image is processed with morphological 'close' to connect the pixels located closer than the predefined threshold. This image is used to extract important parameters, including the centroid location, size and orientation.

The algorithm, which was used to construct the trajectory of each nanoplateform, consists of three consecutive steps applied to each video frame: prediction, measurement and estimation [48,49]. For a given frame  $k$  of a certain trajectory  $i$ , the state of the system was defined as

$$X_k^i := (x_k^i, y_k^i, ux_k^i, uy_k^i, P_k^i), \quad (1)$$

where  $(x, y)$  is the centroid location,  $(u_x, u_y)$  is the centroid velocity and  $P$  is the visibility (related to the probability of detection). The state  $X_k$  was set to be a function of only the previous state  $X_k^i$ , according to the Markovian assumption. In the following description of the processing steps, the index  $i$  was omitted for simplicity.

In the initialization step ( $k = 0$ ), all the detected nanoplateforms from the first frame were used to initialize the trajectories with centroid location at  $(x_0, y_0)$ , initial velocities which were set to 0 and visibilities of 1. In the prediction step ( $k \geq 0$ ), a constant velocity model anticipated the position of the nanoplateforms in the following frame:

$$\begin{aligned} x_{k+1} &= x_k + \Delta t u x_k, & y_{k+1} &= y_k + \Delta t u y_k, \\ u x_{k+1} &= u x_k, & u y_{k+1} &= u y_k, \end{aligned} \quad (2)$$

where  $\Delta t$  denotes the reciprocal of the video frame rate. In the measurement step ( $k \geq 0$ ), we estimated the probability distribution  $f_k(x, y)$  of the location of the nanoplateforms, which was extracted from the filtered frame. For each trajectory, the filtered frame was searched for prominent peaks (close to the locations selected in the prediction step). The brightest of the peaks obtained  $(x_c, y_c)$  (one for each trajectory) were selected and classified into one of three predefined groups: (a) *particles*—bright and prominent peaks; (b) *suspects*—peaks with an average brightness, but still discernible from the background; and (c) *phantoms*—barely visible peaks. For automatic classification, we selected manually two thresholds for brightness,  $T_1$  and  $T_2$  ( $0 < T_2 < T_1 < 1$ ). These thresholds separated the suspects and phantoms among the nanoplateforms.

The estimation step ( $k \geq 0$ ) consisted of the updating of the location of nanoplateforms and the addition of points to appropriate trajectories as follows:

$$(x_{k+1}, y_{k+1}) = \begin{cases} \text{not updated,} & \text{if } P_k > T_1 \text{ and } f_k \leq T_2, \\ \text{does not exist,} & \text{if } P_k \leq T_1 \text{ and } f_k \leq T_2, \\ (x_c, y_c), & \text{otherwise} \end{cases} \quad (3)$$

$$(u x_{k+1}, u y_{k+1}) = \begin{cases} \text{not updated,} & \text{if } P_k > T_1 \text{ and } f_k \leq T_2, \\ \text{does not exist,} & \text{if } P_k \leq T_1 \text{ and } f_k \leq T_2, \\ ((x_c - x_k)/\Delta t, (y_c - y_k)/\Delta t), & \text{otherwise} \end{cases} \quad (4)$$

$$P_{k+1} = \begin{cases} P_k, & \text{if } P_k > T_1 \text{ and } f_k > T_1 \\ \text{does not exist,} & \text{if } P_k \leq T_2 \text{ and } f_k \leq T_1 \\ 2 P_k, & \text{if } P_k \leq T_1 \text{ and } f_k > T_1 \\ 0.5 P_k, & \text{otherwise} \end{cases} \quad (5)$$

where  $(x_c, y_c)$  is the centroid location of the closest bright peak, obtained in the measurement step. The following remarks should be noted. (a) The option ‘does not exist’ in the preceding expressions means that the trajectory is terminated; the option ‘not updated’ means that, in the following frame, the predicted values will be used. (b) The bright peaks that were not used in

constructing the trajectories initialize new trajectories (see the initialization step). (c) The prediction, measurement and estimation steps are repeated for all video frames. In this way, the trajectories of the centroids are obtained, and the robust statistics tools, including rejection of outliers and variance analysis, are used to explore further the constructed trajectories of the nanoplateforms.

#### 2.4. Implementation of an algorithm in the analysis of the nanostructure trajectories

The flow trajectories are determined by several forces, namely the magnetic force ( $F_{mx}$ ,  $F_{my}$ ), viscous fluidic force ( $F_{fx}$ ,  $F_{fy}$ ), nanoplateform–blood cell interactions, gravitational force, buoyancy force, inertial force, and magnetic-dipole or van der Waals inter-nanoplateform forces. The inter-nanoplateform forces can be ignored, since the total volume occupied by the nanoplateforms per unit volume of a fluid is very small. The buoyancy and the inertial force acting on the nanoplateform are evaluated as  $2.19 \times 10^{-6}$  pN and  $1.84 \times 10^{-6}$  pN, respectively, rendering them several orders of magnitude smaller than the other forces. The buoyancy force was calculated according to the relation  $F_b = V_g (\rho_f - \rho_b)$  and the gravity force was calculated according to the relation  $F_g = \rho_b V_g \cdot \rho_f$ , where  $\rho_b$  is the density of the fluid and the conjugate structure, respectively;  $\rho_b = 6.67 \text{ g cm}^{-3}$ , an average density of the PbSe and Fe<sub>2</sub>O<sub>3</sub> nanoparticles;  $V$  is the conjugate volume and  $g$  is the gravity constant. In such a vertical flow, the gravitational force is also ignored. Based on these evaluations, this study should consider mainly the magnetic and fluidic forces (as labeled in the inset of figure 2(B)), while the nanoplateform–blood interactions are already taken into consideration by measuring the nanoplateform transport through fluids with different viscosities.

The fluidic force is obtained using a Stokes approximation of a drag force acting on a nanoplateform, and for simplicity, assuming a spherical shape [50]:

$$F_f = -6\pi\eta R_p(v_p - v_f), \quad (6)$$

where  $\eta$  is the fluid viscosity,  $R_p$  is the nanoplateform's radius,  $v_p$  is the nanoplateform's velocity and  $v_f$  is the fluid's velocity. Considering a motion in the  $x$ - $y$  plane (see figure 2(B)), the components of the fluidic force can be defined as

$$F_{fx} = -6\pi\eta R_p v_{px} \quad (v_{fx}=0), \quad (7)$$

$$F_{fy} = -6\pi\eta R_p(v_{py} - v_{fy}). \quad (8)$$

The total magnetic force acting on the nanoplateforms is equal to a sum of the magnetic forces acting on each individual nanoplateform [51]:

$$F_m = \mu_0 N_{mp} V_{mp} \frac{3\chi_{mp}}{(\chi_{mp}+3)} (H \cdot \nabla) H, \quad (9)$$

where  $N_{mp}$  is the total number of nanoplateforms,  $V_{mp}$  is their volume,  $H$  is the applied magnetic field,  $\chi_{mp}$  is the nanoplateforms' susceptibility, as measured previously by superconducting interference device (SQUID) measurements [43], and  $\mu_0 = 4\pi \times 10^{-7} \text{ H m}^{-1}$  is the air permeability.  $N_{mp}$  was evaluated by counting the number of nanoplateforms that passed through a cross section of the channel per unit time (using the microscope user-friendly program (see section 4)). Furthermore, the total magnetic force acting on the nanoplateforms depends on the

mutual distance between the external magnetic field source and the center of the flow channel (labeled 'd' in figure 2). Thus, the total magnetic forces in the  $x$  and  $y$  directions are given by the following equations [52]:

$$F_{mx}(x, y) = \mu_0 N_{mp} V_{mp} \frac{3\chi_{mp}}{\chi_{mp} + 3} \times \left[ H_x(x, y) \frac{\partial H_x(x, y)}{\partial x} + H_y(x, y) \frac{\partial H_x(x, y)}{\partial y} \right] \quad (10)$$

and

$$F_{my}(x, y) = \mu_0 N_{mp} V_{mp} \frac{3\chi_{mp}}{\chi_{mp} + 3} \times \left[ H_x(x, y) \frac{\partial H_y(x, y)}{\partial x} + H_y(x, y) \frac{\partial H_y(x, y)}{\partial y} \right] \quad (11)$$

$H_x$  and  $H_y$  correspond to the Cartesian component of the magnetic field. The source magnet has a radius  $R_{mag}$  (4.2 cm) and magnetization  $M_s$  of  $1 \times 10^6 \text{ Am}^{-1}$  (a value supplied by the consumer). Thus, the magnetic field gradient felt by the nanoplateforms, at a distance,  $d$ , from the magnet center, and in the  $x$ - $y$  plane, is given by the following equations [51]:

$$H_x(x, y) = \frac{M_s R_{mag}^2}{2} \frac{((x+d)^2 - y^2)}{((x+d)^2 + y^2)^2} \quad (12)$$

$$H_y(x, y) = \frac{M_s R_{mag}^2}{2} \frac{2((x+d)y)}{((x+d)^2 + y^2)^2}. \quad (13)$$

Substitution of equations (12) and (13) into equations (10) and (11), leads to the expressions that describe the magnetic forces in the  $x$  (equation (14)) and  $y$  (equation (15)) directions, respectively:

$$F_{mx} = - \frac{3\mu_0 N_{mp} V_{mp} \chi_{mp} M_s^2 R_{mag}^4}{\chi_{mp} + 3} \frac{(x+d)}{2((x+d)^2 + y^2)^3} \quad (14)$$

$$F_{my} = - \frac{3\mu_0 N_{mp} V_{mp} \chi_{mp} M_s^2 R_{mag}^4}{\chi_{mp} + 3} \frac{y}{2((x+d)^2 + y^2)^3}. \quad (15)$$

The trajectories of nanoplateforms are expressed as the distance traveled in the  $y$  direction versus that in the  $x$  direction. Representative trajectory plots of several nanoplateforms measured in a fluid with a viscosity of 1.73 cP, are shown in figure 5(A). The position of the nanoplateforms were followed one frame after the other, equipositioned by the GUI (see section 2.3), while a trajectory was drawn only for those nanoplateforms that do not disappear for more than three consecutive frames. These trajectories show a progress in the  $y$  direction (along the channel axis) of hundreds of microns during an average time of 10 s.

The representative weighted frequency of appearance over 300 consecutive frames versus the deviation angle,  $\theta$ , of the trajectory with respect to the chamber axis is plotted in figure 5(B).

The deviation is averaged around  $90^\circ$  when measured with the influence of an external magnetic field. Similar plots were drawn for measurements taken at eight different flow rates, six different viscosities, and with and without an external magnetic field. Thus, 96 different plots in all, each supplying a distinct  $\theta$ .

The representative weighted frequency appearance over 300 consecutive frames versus the velocity of the nanoplateforms (as derived by the algorithm mentioned) is plotted in figure 5 (C), revealing an average velocity of  $48 \mu\text{m s}^{-1}$  (when measured in a fluid with a viscosity of 1.73 cP). Thus, the average velocities of the nanoplateforms, in fluids of six different viscosities and eight different flow rates, were derived in a similar manner when measured with and without the influence of the magnetic field gradient. Thus, a correlation between progression distance, directionality ( $\theta$ ) and the average nanoplateforms' velocity, with/without an external magnetic field, could be derived.

The dependence of the deviation of the trajectories with and without an external magnetic field from the channel axis,  $\Delta\theta$  (radians), on the volumetric flow rate ( $\text{ml h}^{-1}$ ), at a variety of viscosities values, is shown in figure 6. Each point on the graph was derived from similar plots to that shown in figure 5(B). The dependence presents a similar behavior when measured at different viscosities, showing a drastic change at relatively low flow rates, though, reaching a plateau with a minor change in the directionality of the trajectories, at flow rates  $>0.2 \text{ml h}^{-1}$ , even in the presence of an external magnetic field.

Obviously, the directionality of the trajectory shown in figure 6, and the velocities and motion presented in figure 5 are determined by the forces acting on the nanoplateforms during a flow, as given in equations (7), (8), (14) and (15). For example, the fluidic force (pN) in the  $x$  direction, derived from equation (7), versus the volumetric flow rate, is plotted in figure 7(A) for several fluid viscosities, as given in the legend of the figure. The magnetic force in that direction, independent of the viscosity parameter (see equation (14)), is plotted by the brown line. These plots suggest that, in most cases, the magnetic force is larger than the fluidic force in the  $x$  direction (see the inset in figure 2(B)), meaning that the magnetic force dominates the trajectory of the nanoplateforms. The magnetic force dominance of the trajectory direction is reduced only at relatively high viscosities and large flow rates.

Figure 7(B) represents plots of the total force acting on the nanoplateforms, including the magnetic and fluidic forces in the  $y$  direction (along the channel), versus the volumetric flow rate. The total force was calculated using equations (8) and (15), when the velocity parameters were extracted from the statistical plots shown in figure 5(C). The total force acting in the  $y$  direction has an additive contribution, both from the fluidic and magnetic forces, so accelerating the nanoplateforms in this direction. When large viscosity demands the application of a larger total force, as well as a larger flow rate, induces a larger force on the nanoplateform in the  $y$  direction. These results have immediate practical consequences regarding the potential application of the nanoplateforms as drug delivery moieties, indicating the possible parameters that could administer a cargo and drug complex into the body. Clearly, the blood stream is a more complex fluid than the polymer solution employed in this study. Thus, additional research is necessary to achieve a more accurate experimental model. Nevertheless, this work represents a significant attempt to tackle this important issue, resulting in concrete, quantitative relationships between nanoplateform size, fluid viscosity, flow rates, external magnetic field strength and their effects on the nanoplateform trajectories.

### 3. Summary

In summary, this study is the first of its kind regarding the quantitative treatment of various crucial aspects related to the potential application of PbSe- $\text{Fe}_2\text{O}_3$  conjugate nanoparticles as *in vivo*, active drug targeting and delivery platforms. We studied the motion of these conjugate

structures in aqueous, viscous flows and in the presence of an external magnetic field and developed quantitative relationships between particle size, fluid viscosity, fluid flow rates and magnetic field strengths, and their effects on the particle trajectories and particle cohesion. Moreover, we have demonstrated that, at magnetic fields of  $\sim 1$  T applied to the flow of the nanoplateforms (of the same order of magnitude found in some common MRI instruments), the trajectories of the particles ( $\theta$ ) can be controlled, which validates the fundamental drug targeting and delivery strategy using magnetic nanoparticles as the active targeting nanoplateforms.

## 4. Methods

### 4.1. Synthesis and characterization

The synthesis of individual PbSe NQDs, stabilized by organic surfactants (oleic acid (OA), and trioctylphosphine (TOP)) was reported in earlier studies [53,54]. This procedure produced nearly monodispersed NQDs with a  $<5\%$  size distribution, and average sizes ranging between 3 and 9 nm, controlled by the reaction temperature and duration. The PbSe NQDs, stabilized with an organic surfactant, were transferred into the aqueous environment by exchanging the OA ligands with positively charged molecules of 2-aminoethanethiol (AET), using a previously reported exchange procedure [14].

The synthesis of the individual  $\gamma$ -Fe<sub>2</sub>O<sub>3</sub> NPs stabilized by organic surfactants (OA and TOP) was performed by a similar procedure to that described by Held *et al* [55]. The  $\gamma$ -Fe<sub>2</sub>O<sub>3</sub> NPs were transferred into an aqueous solution by replacing the organic ligands (AO) with negatively charged hydrate-octakis(tetramethylammonium) (C<sub>32</sub>H<sub>96</sub>N<sub>8</sub>O<sub>20</sub>Si<sub>8</sub>·xH<sub>2</sub>O) molecules, known as the hydrophilic polyhedral silsesquioxane (PSS), via an exchange procedure similar to that given by Benjamin *et al* [56].

The structural and morphological properties of the conjugates studied were examined using a transmission electron microscope (TEM), Tecnai T12, operating at 120 kV with magnification of 52 000. A Jasco V-570 UV/vis/NIR spectrophotometer was used to obtain the absorption of the PbSe NQDs. The room temperature continuous-wave (CW) PL spectra of the PbSe NQD- $\gamma$ -Fe<sub>2</sub>O<sub>3</sub> NP conjugate (suspended either in water or 2,2,4,4,6,8,8,-heptamethyl-nonane glassy solution) were obtained by exciting the samples with a Ti:sapphire laser, while emission was recorded using an Acton monochromator equipped with a charge-coupled device (CCD).

The magnetic properties of the PbSe NQD- $\gamma$ -Fe<sub>2</sub>O<sub>3</sub> NP conjugate structures were studied by using a field-shielded superconducting quantum interference device (SQUID) magnetometer MPMS<sub>2</sub>, controlled by MultiVu software (Quantum Design Inc.) The preparation of the samples is reported in a previous study [43], while the magnetic susceptibility dependence versus the strength of the external magnetic field was measured at a constant temperature, with a stability of  $\Delta T < 0.005$  T, varying the field strength between  $-10\ 000$  Oe  $\leq H \leq 10\ 000$  Oe.

### 4.2. Flow experimental set-up

The preparation of the QD-NP nanoplateforms involved the mixing of equal volumes of the water-based suspensions of PbSe NQDs and  $\gamma$ -Fe<sub>2</sub>O<sub>3</sub> NPs [14,54–56]. The details regarding this process were discussed previously [14]. The average size of the conjugate structures is 33 nm with standard deviation of 12 nm.

The viscosity of the solutions was measured by an ARES 2000 Rheometric Scientific Rheometer.

The system used to analyze the movement of the nanoplateforms was NANOSIGHT LM10™. The system includes a Class I laser device comprised of a small Al metal housing (92 mm ×

66 mm × 47 mm) containing a solid state, single-mode laser diode (<20 mW, 655 nm) configured to launch a finely focused beam through the 500 μl sample chamber. An upper optical window was mounted in a detachable stainless steel top-plate through which the sample was viewed down the microscope. Particles in the liquid sample that pass through the beam path are seen down the microscope as small points of light moving rapidly under the influence of the flow.

The motion of the nanoplateforms was filmed by an AVT Marlin F-033B CCD camera with 10 s exposure duration for each film. The videos were then analyzed using the specially designed software, from which the velocity distribution, flow direction and the trajectories of each conjugate structure could be separately determined.

## Acknowledgments

This work was supported by the Marie Curie Grant Program of the European Union (for both AT and RT), and the Israel Science Foundation (to RT), grant nos. 650/06 and 1182/09. Additional support for this work was received through grants from NSF, AFOSR, ARO and MURI, as well as by a grant from NIH (NAC P41 RR-13218). This work is part of the National Alliance for Medical Image Computing (NAMIC), funded by the National Institutes of Health through the NIH Roadmap for Medical Research, grant U54 EB005149. Information on the National Centers for Biomedical Computing can be obtained from <http://nihroadmap.nih.gov/bioinformatics>.

## References

1. Jain KK. *Curr. Opin. Mol. Ther* 2007;9:563–571. [PubMed: 18041667]
2. Zheng G, Chen J, Stefflova K, Jarvi M, Li H, Wilson BC. *Proc. Natl Acad. Sci. USA* 2007;104:8989. [PubMed: 17502620]
3. Safavy A, Raisch KP, Mantena S, Sanford LL, Sham SW, Krishna NR, Bonner JA. *J. Med. Chem* 2007;50:6284–6288. [PubMed: 17973470]
4. Rhyner MN, Smith AM, Gao X, Mao H, Yang L, Nie S. *Fut. Med.—Nanomed* 2006;1:209–217.
5. Mulder WJM, Griffioen AW, Strijkers GJ, Cormode DP, Nicolay K, Fayad ZA. *Future Med.—Nanomed* 2007;2:307–324.
6. Wan J, Cai W, Meng X, Liu E. *Chem. Commun* 2007;47:5004.
7. Tromsdorf UI, et al. *Nano Lett* 2007;7:2422–2427. [PubMed: 17658761]
8. Hoehn M, Wiedermann D, Justicia C, Ramos-Cabrer P, Kruttwig K, Farr T, Himmelreich U. *J. Physiol* 2007;584:25–30. [PubMed: 17690140]
9. Frullano L, Meade TJ. *J. Biol. Inorg. Chem* 2007;12:939–949. [PubMed: 17659368]
10. Andreev AD, Lipovskii AA. *Phys. Rev. B* 1999;59:15402.
11. Du H, Chen C, Krishnan R, Krauss TD, Harbold JM, Wise FW, Thomas MG, Silcox J. *Nano Lett* 2002;2:1321–1324.
12. Wehrenberg BL, Wang CJ, Guyot-Sionnest P. *J. Phys. Chem. B* 2002;106:10634–10640.
13. Schaller RD, Klimov VI. *Phys. Rev. Lett* 2004;92 186601.
14. Etgar L, Lifshitz E, Tannenbaum R. *J. Phys. Chem. C* 2007;111:6238–6244.
15. Steckel JS, Coe-Sullivan S, Bulović V, Bawendi MG. *Adv. Mater* 2003;15:1862–1866.
16. Gaponik N, Radtchenko IL, Gerstenberger MR, Fedutik YA, Sukhorukov GB, Rogach AL. *Nano Lett* 2003;3:369–372.
17. Santoni A, Paolucci G, Santoro G, Prince KC, Christensen NE. *J. Phys.: Condens. Matter* 1992;4:6759–6768.
18. Alivisatos AP. *J. Phys. Chem* 1996;100:13226–13239.
19. Kagan CR, Murray CB, Bawendi MG. *Phys. Rev. B* 1996;54:8633.
20. Kim S, et al. *Nat. Biotechnol* 2004;22:93–97. [PubMed: 14661026]
21. Sargent EH. *Adv. Mater* 2005;17:515.
22. Lifshitz E, et al. *J. Phys. Chem. B* 2006;110:25356–25365. [PubMed: 17165982]
23. Klimov VI, McGuire JA, Schaller RD, Rupasov VI. *Phys. Rev. B* 2008;77 195324.

24. Forbes ZG, Yellen BB, Barbee KA, Friedman G. *IEEE Trans. Magn* 2003;39:3372–3377.
25. Asmatulu R, Zalich MA, Claus RO, Riffle JS. *J. Magn. Magn. Mater* 2005;292:108–119.
26. Dobson J. *Drug Dev. Res* 2006;67:55–60.
27. Jain KK. *Technol. Cancer Res. Treat* 2008;7:1–14. [PubMed: 18198919]
28. Voltz E, Gronemeyer H. *Int. J. Biochem. Cell Biol* 2008;40:1–8. [PubMed: 17951100]
29. Duguet E, Vasseur S, Mornet S, Devoisselle JM. *Future Med.—Nanomed* 2006;1:157–168.
30. Iqbal SS, Mayo WM, Bruno JG, Bronk BV, Batt CA, Chambers JP. *Biosens. Bioelectron* 2000;15:549–578. [PubMed: 11213217]
31. Popplewell J, Sakhnini L. *J. Magn. Magn. Mater* 1995;149:72–78.
32. Raj K, Moskowitz B, Casciari R. *J. Magn. Magn. Mater* 1995;149:174–180.
33. Molday RS, Mackenzie D. *J. Immunol. Methods* 1982;52:353–367. [PubMed: 7130710]
34. Jung CW, Jacobs P. *Magn. Reson. Imag* 1995;13:661–674.
35. Medintz IL, Uyeda HT, Goldman ER, Mattoussi H. *Nat. Mater* 2005;4:435–446. [PubMed: 15928695]
36. Kulkarni DP, Das DK, Chukwu GA. *J. Nanosci. Nanotechnol* 2006;6:1150–1154. [PubMed: 16736780]
37. Kim J, Piao Y, Hyeon T. *Chem. Soc. Rev* 2009;38:372–390. [PubMed: 19169455]
38. Jin X, Zhao Y, Richardson A, Moore L, Williams PS, Zborowski M, Chalmers JJ. *Anal* 2008;133:1767–1775.
39. Zhang H, Moore LR, Zborowski M, Williams PS, Margel S, Chalmers JJ. *Anal* 2005;130:514–527.
40. Zborowski M, Oстера GR, Moore LR, Milliron S, Chalmers JJ, Schechter AN. *Biophys. J* 2003;84:2638–2645. [PubMed: 12668472]
41. Nakamura N, Zborowski M, Lasky LC, Margel S, Chalmers JJ. *Exp. Fluids* 2001;30:371–380.
42. Chalmers JJ, Zhao Y, Nakamura M, Melnik K, Lasky L, Moore L, Zborowski M. *J. Magn. Magn. Mater* 1999;194:231–241.
43. Etgar L, Leitun G, Fradkin L, Assaraf YG, Tannenbaum R, Lifshitz E. *ChemPhysChem* 2009;10:2235–2241. [PubMed: 19630057]
44. Kachouie NN, Fieguth P, Ramunas J, Jervis E. *Int. J. Biomed. Imag* 2006;2006:1–10.
45. Acton ST, Wethmar K, Ley K. *Microvas. Res* 2002;63:139–148.
46. Helmuth JA, Burckhardt CJ, Koumoutsakos P, Greber UF, Sbalzarini IF. *J. Struct. Biol* 2007;159:347–358. [PubMed: 17532228]
47. Bar-Shalom, Y.; Fortmann, TE. *Tracking and Data Association*. Boston, MA: Academic; 1988.
48. Rathi Y, Vaswani N, Tannenbaum A. *IEEE Trans. Image Process* 2007;16:1370–1382. [PubMed: 17491466]
49. Michailovich O, Tannenbaum A. *IEEE Trans. Image Process* 2008;17:847–856. [PubMed: 18482881]
50. Batchelor, GK. *An Introduction to Fluid Dynamics*. London: Cambridge University Press; 1970.
51. Furlani EP, Ng KC. *Phys. Rev. E* 2006;73 061919.
52. Furlani EJ, Furlani EP. *J. Magn. Magn. Mater* 2007;312:187–193.
53. Yu WW, Falkner JC, Shih BS, Colvin VL. *Chem. Mater* 2004;16:3318–3322.
54. Brumer M, Kigel A, Amirav L, Sashchiuk A, Solomesh O, Tessler N, Lifshitz E. *Adv. Funct. Mater* 2005;15:1111–1116.
55. Euliss LE, Grancharov S, O'Brien S, Deming TJ, Stucky GD, Murray CB, Held GA. *Nano Lett* 2003;3:1489–1493.
56. Frankamp BL, Fischer NO, Hong R, Srivastava S, Rotello VM. *Chem. Mater* 2006;18:956–959.

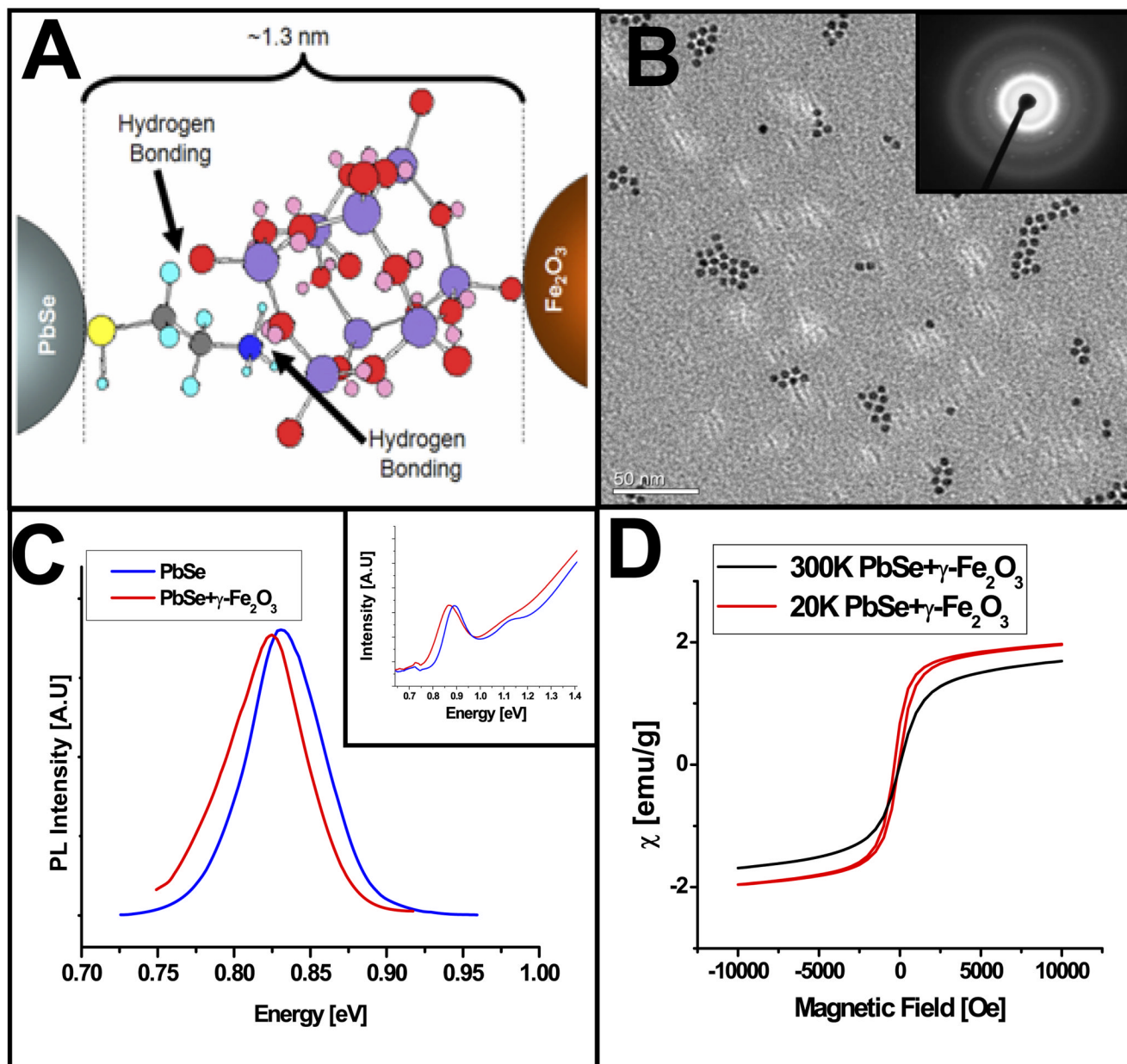


**Figure 1.**

(A) Schematic representation of the chemical connection between the PbSe QDs to the  $\gamma$ - $\text{Fe}_2\text{O}_3$  NPs; (B) transmission electron microscope (TEM) image of PbSe QD- $\gamma$ - $\text{Fe}_2\text{O}_3$  NP nanoplateforms, deposited onto a TEM grid from the acidic solution at pH  $\sim$  5, showing clustering of particles into a platform with an average size of  $30 \pm 10$  nm. A corresponding electron diffraction pattern, shown in the inset, reveals the existence of PbSe and  $\gamma$ - $\text{Fe}_2\text{O}_3$  particles within a cluster; (C) representative PL spectra of individual PbSe NQDs (blue curve) and of the NQD-NP conjugates (red curve). The spectra were recorded at room temperature. Corresponding absorption spectra of individual PbSe NQDs (blue curve) and of NQD-NP conjugates (red curve) are shown in the inset. The average diameters of the NQDs and the NPs were 5 nm; (D) plots of the magnetic susceptibility ( $\chi$ ) versus strength of an external magnetic

field of the PbSe NQD- $\gamma$ -Fe<sub>2</sub>O<sub>3</sub> NP nanoplatforms. The plots were recorded at 20 and 300 K, as indicated in the figure legends.

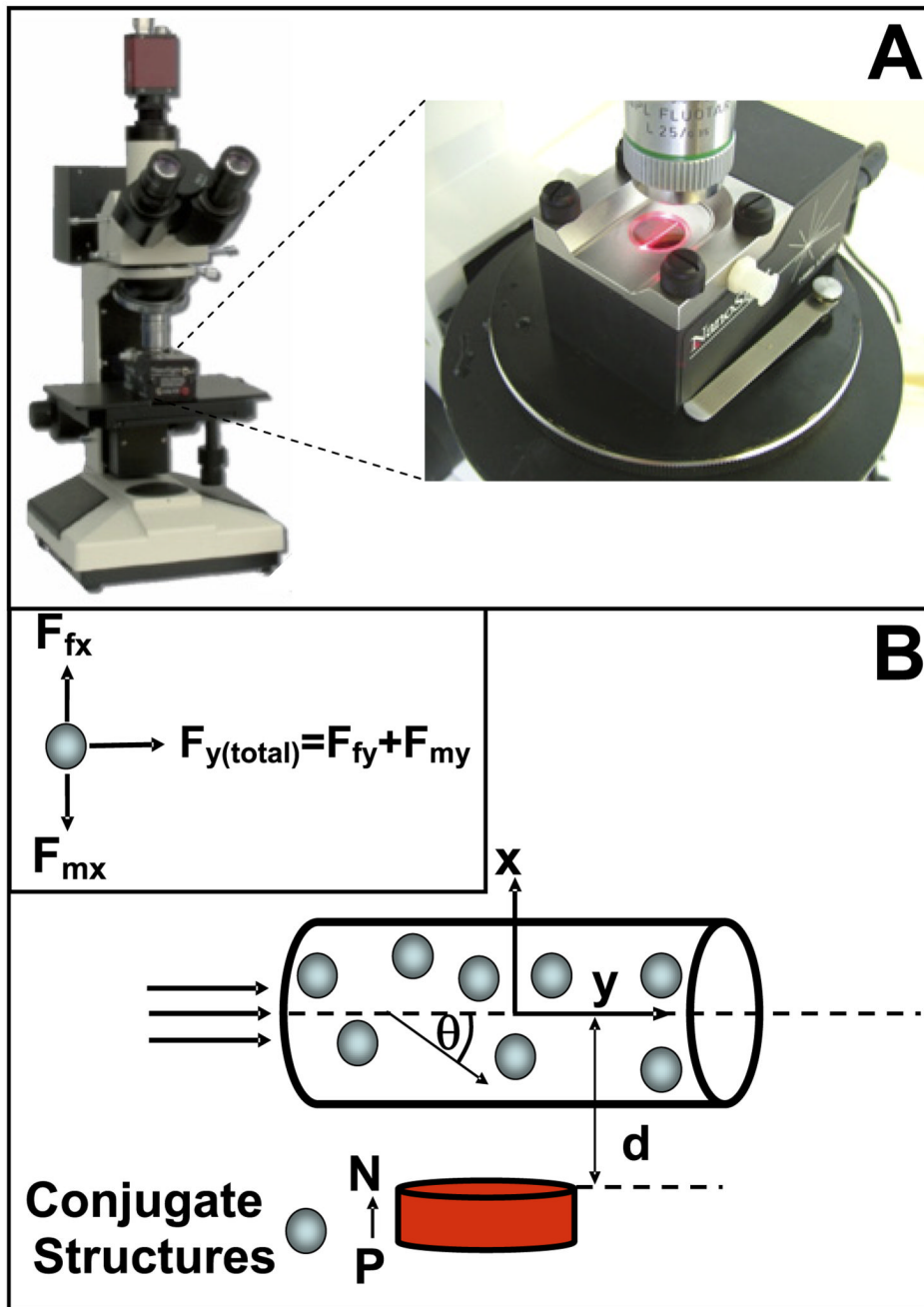


**Figure 2.** (A) A photograph of the flow set-up; (B) the schematic representation of the experimental set-up and the distribution of forces on the nanoplateforms in the viscous flow. The distance between the magnet and the center of the channel is represented by  $d$  and equal to 5.5 cm. The forces acting on each nanoplateform in the  $x$  direction are the difference between the fluidic force ( $F_{fx}$ ) and the magnetic force ( $F_{mx}$ ), and in the  $y$  direction the total force is the sum of the fluidic force ( $F_{fy}$ ) and the magnetic force ( $F_{my}$ ), since both components act on the nanoplateform in the same direction.

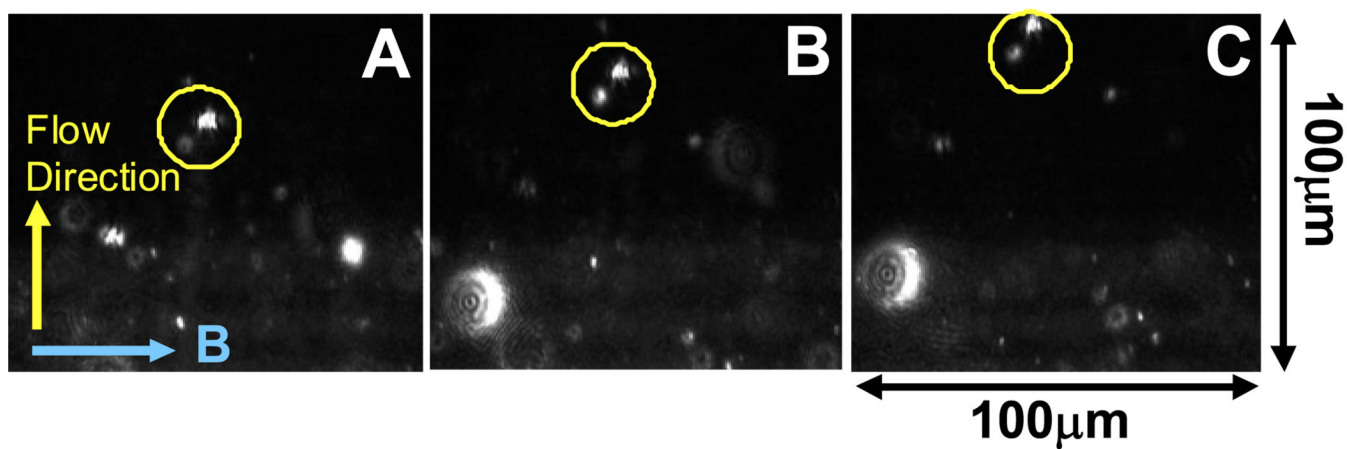


**Figure 3.** (A)–(C) Representative images of nanoplateforms' trajectories as visualized during a flow, tracking the position change of the two selected nanoplateforms (see yellow circles in the figure). The fluid viscosity of this sample was 1.73 cP and the flow rate was  $0.9 \text{ ml h}^{-1}$  under an external magnetic field  $B$ .

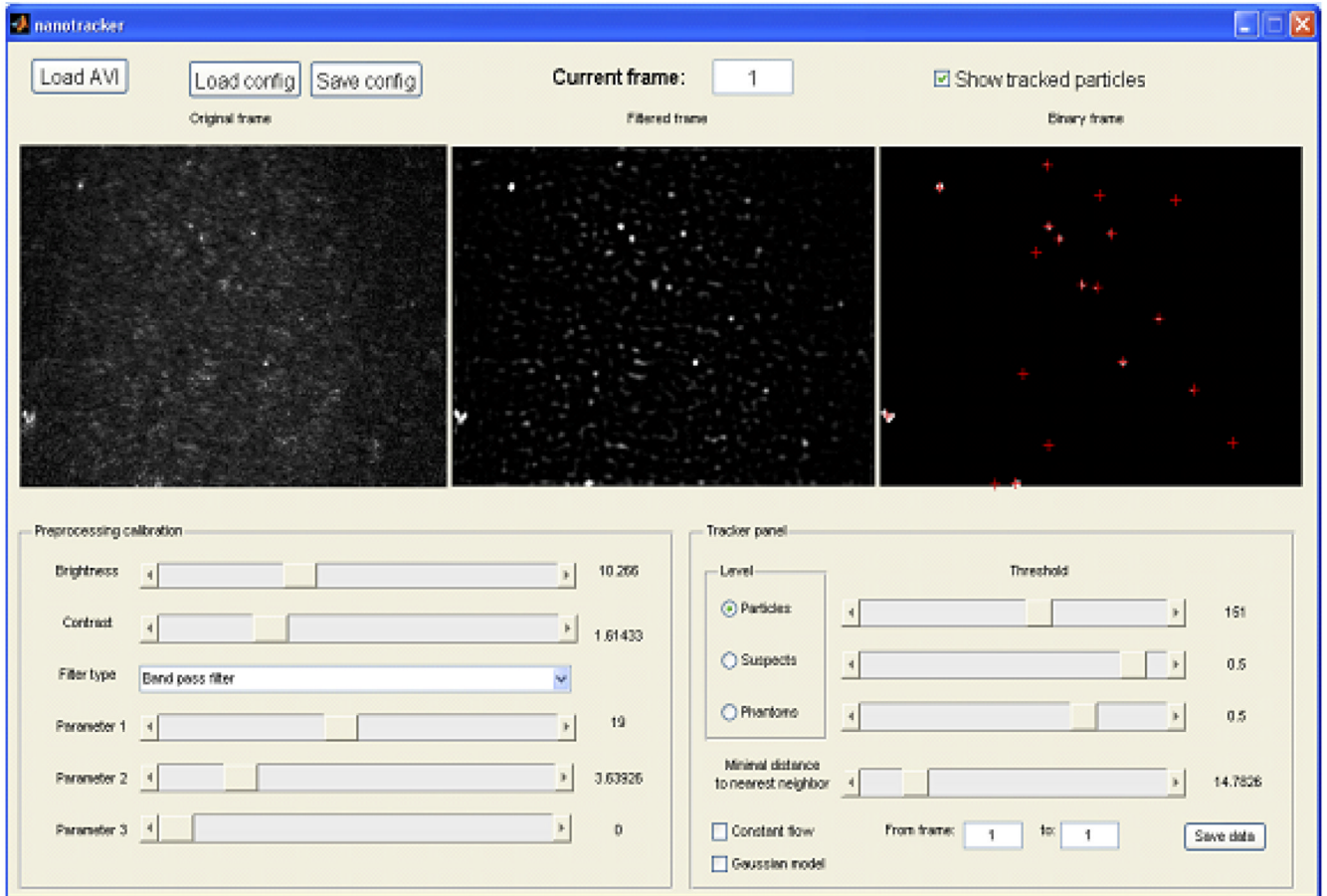


**Figure 4.** The 'nanotracker' graphical user interface. The three images show the progression of the image processing and tracking procedure onscreen. The left image is the original noisy image with poor contrast, the middle image is the filtered preprocessed image and the right image is the binary decision image that exhibits the detected centroid locations of particle groups marked by the red cross.

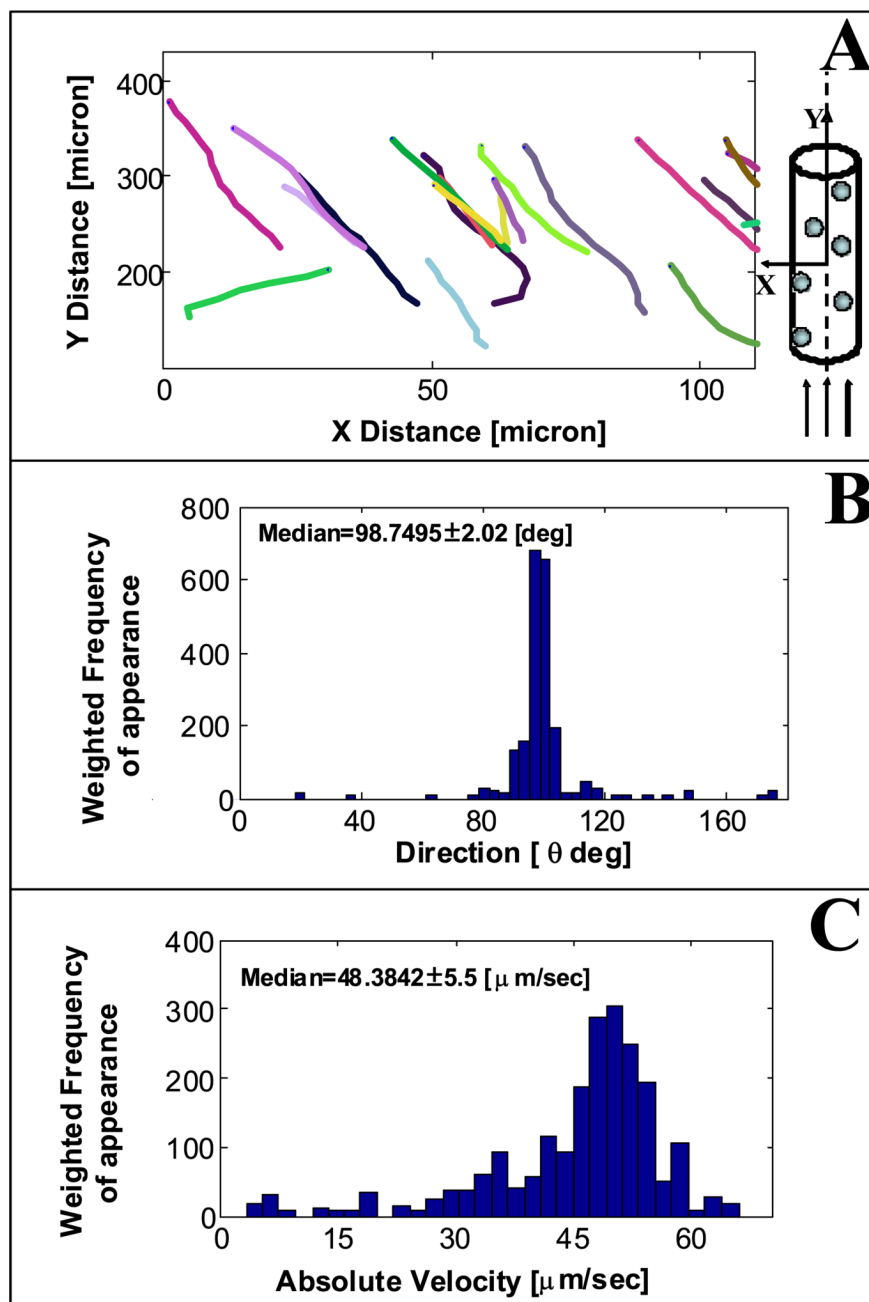


**Figure 5.** (A) Representative trajectory plots of several nanoplatforms; (B) representative weighted frequency of appearance over 300 consecutive frames versus the deviation angle,  $\theta$ , of the trajectory with respect to the chamber axis; (C) representative weighted frequency appearance over 300 consecutive frames versus the velocity of the nanoplatforms (as derived by the algorithm), revealing an average velocity of  $48 \mu\text{m s}^{-1}$ . Measurements were made of a fluid with a viscosity of 1.73 cP and flow rate of  $0.9 \text{ ml h}^{-1}$  under an external magnetic field  $B$ .

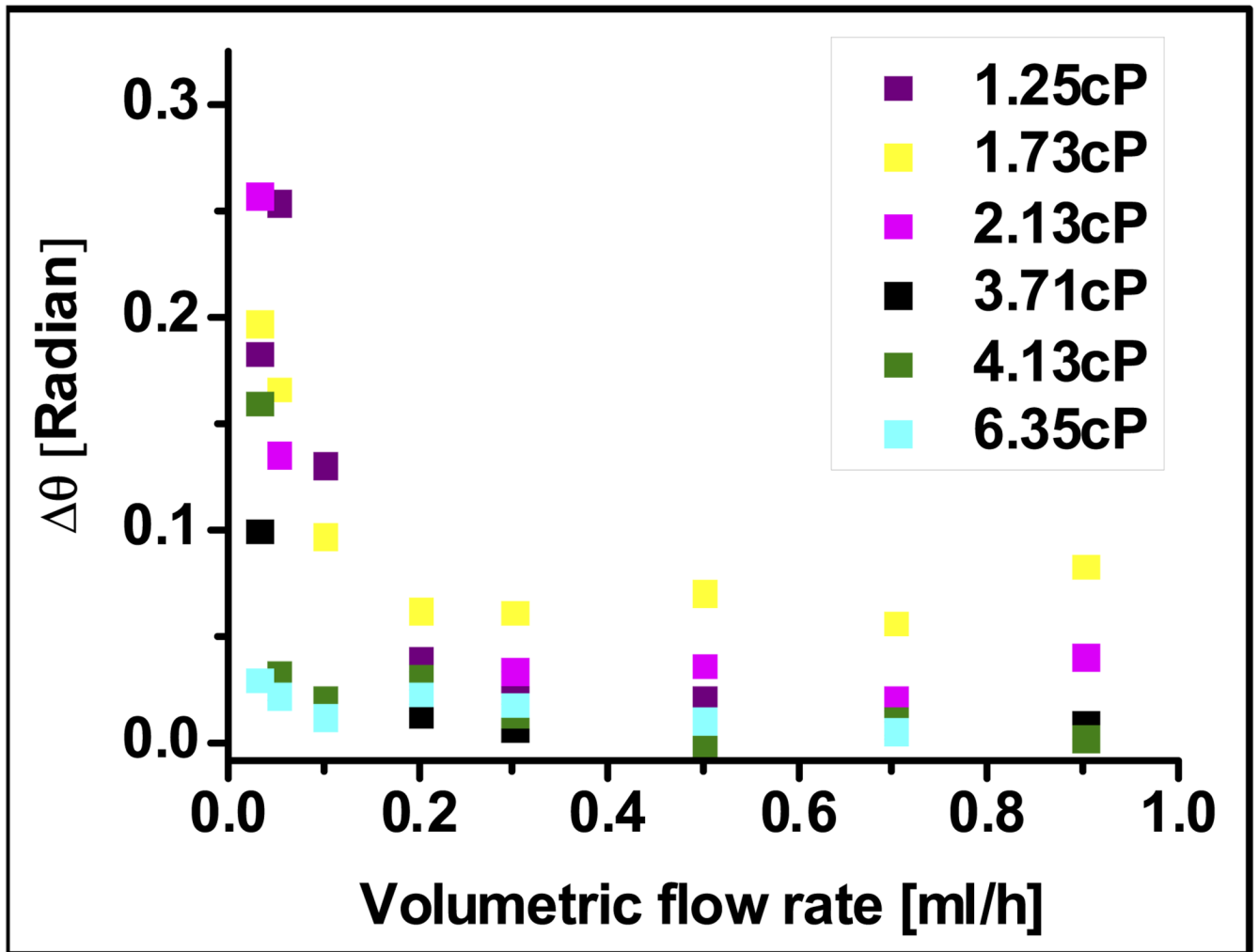


**Figure 6.**

The influence of an external magnetic field on the nanoplatform trajectories. Flow direction differences ( $\Delta\theta$ ) of the conjugate structures in fluids with different viscosities and volumetric flow rates, under an external magnetic field of 1 T. The direction differences were derived from the difference of the deviation between nanoplatforms with and without an external magnetic field.

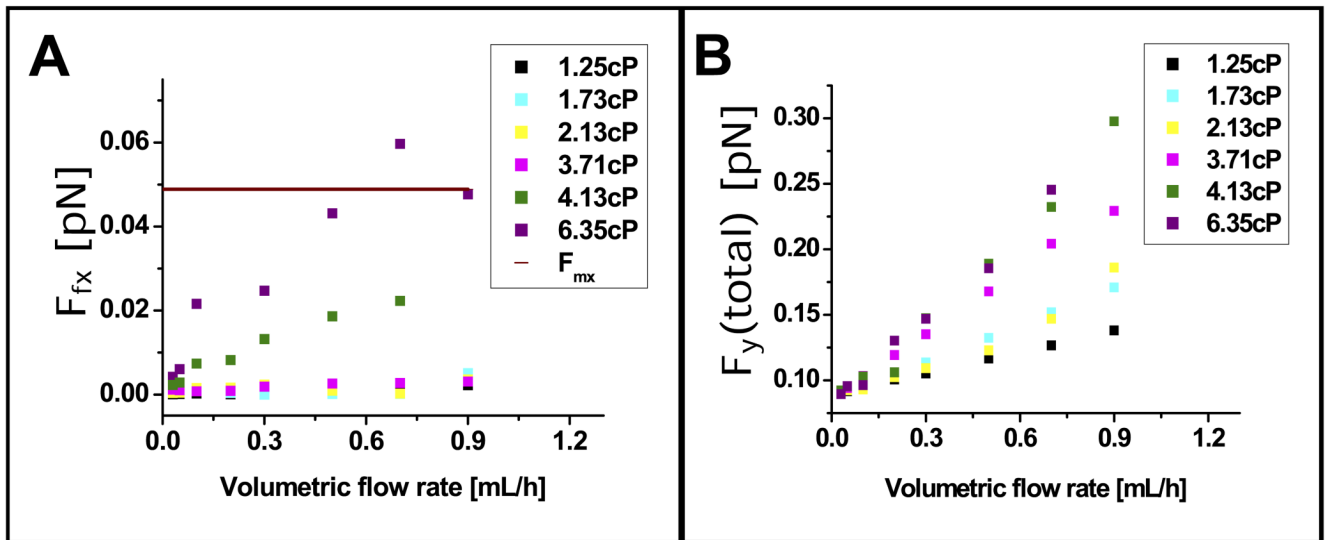


**Figure 7.**

Force balance on the nanoplateforms during their flow. (A) The fluidic and magnetic forces at different viscosities and volumetric flow rates in the  $x$  direction; (B) the total force in the  $y$  direction in fluids with several viscosities and different volumetric flow rates. The total force in the  $y$  direction is the sum of the magnetic and fluidic forces.